

# Large off-diagonal exchange couplings and spin liquid states in $C_3$ -symmetric iridates

Ravi Yadav,<sup>1</sup> Satoshi Nishimoto,<sup>1,2</sup> Manuel Richter,<sup>1,3</sup> Jeroen van den Brink,<sup>1,2</sup> and Rajyavardhan Ray<sup>1,3,\*</sup>

<sup>1</sup>*IFW Dresden, Helmholtzstrasse 20, D-01069 Dresden, Germany*

<sup>2</sup>*Department of Physics, TU Dresden, D-01062 Dresden, Germany*

<sup>3</sup>*Dresden Center for Computational Materials Science (DCMS), TU Dresden, D-01062 Dresden, Germany*



(Received 7 January 2019; revised manuscript received 17 September 2019; published 15 October 2019)

Iridate oxides on a honeycomb lattice are considered promising candidates for realization of quantum spin liquid states. We investigate the magnetic couplings in a structural model for a honeycomb iridate  $K_2\text{IrO}_3$ , with  $C_3$  point-group symmetry at the Ir sites, which is an end member of the recently synthesized iridate family  $K_x\text{Ir}_y\text{O}_2$ . Using *ab initio* quantum chemical methods, we elucidate the subtle relationship between the real space symmetry and magnetic anisotropy and show that the higher point-group symmetry leads to high frustration with strong magnetic anisotropy driven by the unusually large off-diagonal exchange couplings ( $\Gamma$ 's) as opposed to other spin-liquid candidates considered so far. Consequently, large quantum fluctuations imply lack of magnetic ordering consistent with the experiments. Exact diagonalization calculations for the fully anisotropic  $K$ - $J$ - $\Gamma$  Hamiltonian reveal the importance of the off-diagonal anisotropic exchange couplings in stabilizing a spin liquid state and highlight an alternative route to stabilize spin liquid states for ferromagnetic  $K$ .

DOI: [10.1103/PhysRevB.100.144422](https://doi.org/10.1103/PhysRevB.100.144422)

## I. INTRODUCTION

The possibility to realize a spin liquid (SL) state in condensed matter systems is being intensively investigated from both theoretical and experimental standpoints [1–3]. SL states are characterized by large degeneracy in the ground state, suppression of long-range (magnetic) order, and cannot be described by the broken symmetries associated with conventional magnetic ground states [4]. In this regard, most promising candidates are the spin-orbit-driven Mott insulators on a honeycomb lattice [5], such as  $\text{Na}_2\text{IrO}_3$  [6,7],  $\alpha$ - $\text{Li}_2\text{IrO}_3$  [8,9], and  $\alpha$ - $\text{RuCl}_3$  [1,10,11]. Due to  $d^5$  configuration in the presence of octahedral crystal field environment and spin-orbit coupling (SOC), the low-energy electronic properties are typically described by an effective nearest-neighbor Kitaev-Heisenberg Hamiltonian ( $K$ - $J$  Hamiltonian) acting in the  $j_{\text{eff}} = 1/2$  subspace. The large ratio of Kitaev to Heisenberg couplings,  $K/J \gg 1$ , found in these materials imply strong magnetic anisotropy and proximity to a SL state. However, the presence of extended range magnetic couplings and small but finite  $J$  render a long-range magnetic order instead [12–15].

Most of the works in these honeycomb lattice iridates have, therefore, focused on studying the effects of external stimulus, such as magnetic field [11,16], hydrostatic pressure [17–19], and trigonal distortions [15], as well as chemical substitutions and doping [20,21], in order to tune the magnetic couplings favorably for a SL state. Very recently, a new family of honeycomb lattice iridates,  $K_x\text{Ir}_y\text{O}_2$ , has been synthesized and in a substantial range of concentrations, including the end member  $K_2\text{IrO}_3$ , a structural model featuring a  $C_3$  point-group (PG) symmetry at the Ir sites was proposed [22,23]. The magnetic susceptibility measurements suggest that no long-range order

or spin freezing develops down to 1.8 K, while the specific heat is finite at low temperatures, implying the possibility of a gapless quantum SL state [23].

Here, we report the influence of  $C_3$  point-group symmetry at the transition metal ion site on the nearest neighbor (NN) magnetic interactions between Ir atoms. Starting with the proposed structural model for  $K_2\text{IrO}_3$ , we discuss the evolution of the magnetic couplings with deviations from the high symmetry structure and implications for the stability of a SL state. The NN magnetic couplings are obtained using quantum chemistry electronic structure calculations, performed for a crystal structure with optimized atomic positions as obtained within density functional theory (DFT). We find unusually large off-diagonal exchange couplings:  $\Gamma_{xy} \sim 5$  meV and  $\Gamma_{yz} \sim -9$  meV (in the local Kitaev frame), approximately 10 times larger than in  $\text{Na}_2\text{IrO}_3$ . At the same time, while the  $K$  and  $J$  exchange terms are smaller,  $K/J$  ratio is comparable to other honeycomb iridates, thus motivating a  $K$ - $J$ - $\Gamma$  Hamiltonian as an appropriate model to capture the underlying physics in  $K_2\text{IrO}_3$ . We identify the origin of such large  $\Gamma$ 's as constraints on the relative orientation of the O-O pairs within the  $\text{IrO}_6$  octahedra due to  $C_3$  PG symmetry at the Ir sites imposed by the large K ions. The large  $\Gamma$ -driven magnetic anisotropy implies strong magnetic frustration and is responsible for suppression of magnetic ordering, observed experimentally.

We note that there is an emerging consensus regarding the importance of  $\Gamma$  terms in understanding the magnetic interactions in honeycomb lattice Mott insulators. Therefore, models involving such terms are being investigated. For example, an anisotropic  $\Gamma$  as well as a  $K$ - $\Gamma$  model on a honeycomb lattice support a SL state [24,25]. The  $\Gamma$  terms are also found to be important in explaining the recent neutron scattering and high-temperature magnetic susceptibility experiments in  $\alpha$ - $\text{RuCl}_3$  [26,27]. However, these works consider only one

\*r.ray@ifw-dresden.de

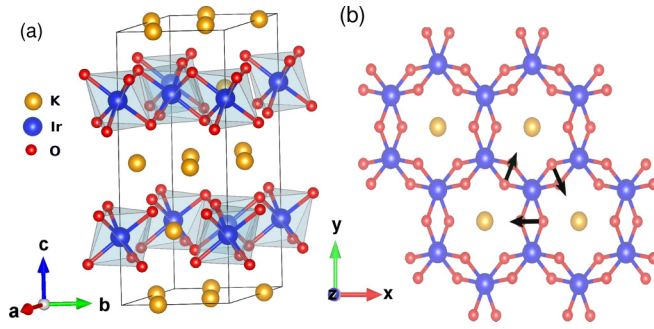


FIG. 1. Crystal structure of  $\text{K}_2\text{IrO}_3$ : (a) shows the alternating layers formed of K ions, and hexagonal network formed by  $\text{IrO}_6$  octahedra with K ions at the center of the hexagons. (b) Top view of the honeycomb plane spanned by the  $\text{IrO}_6$  octahedra and K ions at center. Manifestation of the  $C_3$  PG symmetry: the in-plane projections of the O-O links in each  $\text{Ir}_2\text{O}_2$  plaquette are oriented  $120^\circ$  with respect to each other (shown by arrow from the O atoms above the Ir plane to O atoms below the Ir plane).

component of  $\Gamma$  per bond, as opposed to our findings for the  $C_3$ -symmetric structure.

Our exact diagonalization (ED) calculations using the quantum chemical NN magnetic couplings for  $\text{K}_2\text{IrO}_3$  reveal that the fate of a SL state in the fully anisotropic  $K$ - $J$ - $\Gamma$  Hamiltonian is determined by the relative signs of  $\Gamma_{ij}$ 's: a  $\Gamma$ -driven SL state is found to be stable for small values of  $\Gamma_{ij} < 0$  and spread over a large region in the  $\Gamma_{xy}$ - $\Gamma_{yz}$  plane. Moreover, the ferromagnetic-Kitaev-SL-stripy path of the  $K$ - $J$  model [5] is also recovered at finite  $\Gamma_{ij}$ 's. Further inclusion of extended range Heisenberg couplings suggests competing magnetic orders in  $\text{K}_2\text{IrO}_3$ , which may have interesting implications for magnetism.

## II. RESULTS AND DISCUSSIONS

### A. Structural details

In the proposed structural model,  $\text{K}_x\text{Ir}_y\text{O}_2$  ( $1 \lesssim x/y \lesssim 2$ ) crystallizes in the high symmetry space group  $P6_322$  (no. 182) [22] as opposed to  $C2/m$  for the related iridate  $\text{Na}_2\text{IrO}_3$  [6]. For brevity, we focus on the stoichiometric end member  $\text{K}_2\text{IrO}_3$ , corresponding to  $x = 4/3$  and  $y = 2/3$ . Starting from the experimental values of the external parameters, the atomic positions were optimized using DFT utilizing the space group symmetries (see Appendix A).

The resulting structure features alternating layers of nonmagnetic cations (K ions, in this case) and a two-dimensional/planar honeycomb network of  $\text{IrO}_6$  octahedra. Within the planar honeycomb network, the transition metal (TM) ions span a regular honeycomb lattice and share O-O edges between them (see Fig. 1). Within each honeycomb plane, one K ion is also present at the center of the hexagons. As compared to  $\text{Na}_2\text{IrO}_3$ , the TM-ligand distance  $d_{\text{Ir-O}} = 2.07 \text{ \AA}$  is comparable, while the TM-TM distance  $d_{\text{Ir-Ir}} = 3.05 \text{ \AA}$  and the TM-O-TM angle  $\angle \text{Ir-O-Ir} = 95.06^\circ$  are much smaller (see Appendix A). Further notable differences with the related iridate  $\text{Na}_2\text{IrO}_3$  are (i) the larger interlayer separation: the two Ir (or K) layers are separated by approximately  $6.8 \text{ \AA}$ , as opposed to  $5.6 \text{ \AA}$  in  $\text{Na}_2\text{IrO}_3$ , and (ii)

each  $\text{IrO}_6$  octahedron has a  $C_3$  symmetry about the “ $c$ ” axis centered at the Ir atoms. As a result, a highly symmetric real space structure is realized where the projection of O-O links at every Ir-Ir bond on the honeycomb plane are at  $120^\circ$  relative to each other, as shown in Fig. 1(b).

### B. Electronic properties and magnetic couplings

The Ir- $5d$  levels in the presence of an octahedral ligand field split into  $e_g$  and  $t_{2g}$  levels, with the latter lying at significantly lower energy [28] (also see Appendix A). The large crystal field splitting results in  $t_{2g}^5$  configuration yielding effectively one hole per site. Strong spin-orbit coupling further splits the  $t_{2g}$  states into fully occupied  $j_{\text{eff}} = 3/2$  and half-filled  $j_{\text{eff}} = 1/2$  states [29–31]. Deviations from an ideal octahedral environment may lead to some admixture between these  $j_{\text{eff}}$  states.

The nearest-neighbor (NN) magnetic interactions were derived using quantum chemistry calculations performed on embedded clusters consisting of two edge-shared octahedra ( $\text{Ir}_2\text{O}_{10}$  units) plus their NN octahedral units and NN K ions (see Appendix B). At each Ir-Ir bond in  $\text{K}_2\text{IrO}_3$ , this structural unit has an approximate  $C_{2h}$  point-group symmetry. Since the deviation from the  $C_{2h}$  symmetry is very small (see Appendix A), an antisymmetric Dzyaloshinskii-Moriya (DM) term, which is not allowed in  $C_{2h}$  symmetry due to the presence of an inversion center, is expected to be negligible. Therefore, a generalized bilinear Hamiltonian between a pair of pseudospins  $\tilde{\mathbf{S}}_i$  and  $\tilde{\mathbf{S}}_j$  is obtained for the  $C_{2h}$  symmetry of the structural unit [14]:

$$\mathcal{H}_{ij}^{(\gamma)} = J \tilde{\mathbf{S}}_i \cdot \tilde{\mathbf{S}}_j + K \tilde{S}_i^\gamma \tilde{S}_j^\gamma + \sum_{\alpha \neq \beta} \Gamma_{\alpha\beta} (\tilde{S}_i^\alpha \tilde{S}_j^\beta + \tilde{S}_i^\beta \tilde{S}_j^\alpha), \quad (1)$$

where  $J$  and  $K$  are the Heisenberg and Kitaev exchange couplings, respectively, and  $\Gamma_{\alpha\beta}$  coefficients are the off-diagonal components of the symmetric anisotropic exchange matrix, with  $\alpha, \beta = x, y, z$ . A local Kitaev reference frame is used, such that, for each Ir-Ir bond, the  $z$  coordinate is perpendicular to the  $\text{Ir}_2\text{O}_2$  plaquette.

The magnetic couplings were determined by mapping the *ab initio* data, obtained in the multireference configuration-interaction (MRCI) calculations including spin-orbit effects, onto the above effective spin Hamiltonian [Eq. (1)] following the scheme detailed in Refs. [11,32,33] and outlined in Appendix B. Note that such a computational procedure has been successfully applied to other spin-orbit driven Mott insulators [11,14,20,32–36].

The magnetic couplings thus obtained are listed in Table I. The most striking aspect is the unusually large off-diagonal exchange couplings,  $\Gamma$  terms, approximately 10 times as compared to  $\text{Na}_2\text{IrO}_3$ . This is accompanied by much smaller  $K$  and  $J$ . The ratio  $K/J$ , however, is comparable to the corresponding value in  $\text{Na}_2\text{IrO}_3$ , implying that  $\text{K}_2\text{IrO}_3$  is magnetically very frustrated. This further suggests that the magnetic anisotropy in  $\text{K}_2\text{IrO}_3$  is large and dominated by the  $\Gamma$  terms, unlike any other known spin-orbit-driven Mott insulator on a honeycomb lattice. Consequently, a fully anisotropic  $K$ - $J$ - $\Gamma$  Hamiltonian model would be necessary to describe this system. It is interesting to note that the magnetic couplings listed in Ref. [22] also suggest large off-diagonal

TABLE I. Nearest neighbor magnetic couplings (in meV) for  $\text{K}_2\text{IrO}_3$  and as obtained from spin-orbit MRCI calculations for the DFT-optimized structure. For comparison, the corresponding values for bonds  $B1$  (top) and  $B2$  (bottom) in  $\text{Na}_2\text{IrO}_3$  are also mentioned (taken from Ref. [37]).

$\text{A}_2\text{IrO}_3$	$\angle\text{Ir-O-Ir}$	$K$	$J$	$\Gamma_{xy}$	$\Gamma_{yz} = -\Gamma_{zx}$
$\text{A} = \text{K}$	$95.0^\circ (\times 3)$	-6.3	1.3	<b>5.2</b>	<b>-8.9</b>
$\text{A} = \text{Na}$	$99.5^\circ (\times 1)$	<b>-20.8</b>	<b>5.2</b>	-0.7	-0.8
	$98.0^\circ (\times 2)$	<b>-15.6</b>	<b>2.2</b>	-1.1	0.8

couplings similar to our *ab initio* results. The mismatch in the magnitude of exchange couplings can be attributed to different methods employed, as also noticed in previous studies on honeycomb lattice Mott insulator  $\alpha\text{-RuCl}_3$  [11,38].

### C. Role of $C_3$ symmetry and interlayer species

In order to understand the origin of such large  $\Gamma$ 's, we study the (distinct) structural differences with  $\text{Na}_2\text{IrO}_3$ . The characteristic features of the honeycomb planes in  $\text{K}_2\text{IrO}_3$  are negligible trigonal distortions (due to large interlayer separations) and a regular  $120^\circ$  arrangement of O-O links centered at Ir-Ir bonds when projected on the plane of Ir atoms [see Fig. 1(b)]. Therefore, starting from  $\text{K}_2\text{IrO}_3$ , an approximate lower symmetry structure similar to  $\text{Na}_2\text{IrO}_3$  can be obtained in two steps. First, within the considered  $\text{Ir}_2\text{O}_{10}$  unit, the four outer O-O links are rotated about an axis perpendicular to the Ir plane and centered between the respective O-O links such that the structural unit retains the  $C_{2h}$  symmetry, albeit without the  $C_3$  symmetry about the “ $c$ ” axis at the Ir sites. Due to the  $C_{2h}$  symmetry, these octahedral distortions can be quantified by a single parameter: twist angle  $\phi$  which measures the deviation of the neighboring O-O links with respect to the O-O link in the central  $\text{Ir}_2\text{O}_2$  plaquette (see the inset of Fig. 2). Second, introducing trigonal distortions with the trigonal axis perpendicular to the Ir plane. We consider clusters with different values of  $\phi$  and trigonal distortion. For consistency and comparison, the same point charge embedding was used for all the cases (see Appendix C).

The dependence of the NN magnetic couplings on  $\phi$  is shown in Fig. 2. The strength of the Kitaev exchange ( $\Gamma_{yz}$ ) increases (decreases) away from the constrained case ( $\phi = 0$ ), while  $\Gamma_{xy}$  changes sign. The NN Heisenberg exchange  $J$ , on the other hand, has a qualitatively similar behavior as  $K$ , and lies in the range of 2 meV and 3.7 meV (not shown). The corresponding values for the  $\text{Ir}_2\text{O}_{10}$  structural units of  $\text{K}_2\text{IrO}_3$  and  $\text{Na}_2\text{IrO}_3$  are also shown. The strength of the  $K$  and  $J$  parameters are substantially larger in the presence of trigonal distortion, as evidenced from the values for  $\text{Na}_2\text{IrO}_3$  (filled symbols at  $\phi \approx 8^\circ$  in Fig. 2) and also noted earlier [15]. We emphasize that the magnetic exchange couplings for the  $\text{Ir}_2\text{O}_{10}$  units in Fig. 2 are obtained within the MRCI framework, and thus provide a reliable qualitative estimate on their evolution with  $\phi$ . However, a full quantum chemical treatment of the NN octahedral units is required to obtain a good quantitative estimate of magnetic exchange interactions, as done for the values in Table I (see Appendixes B and C for details).

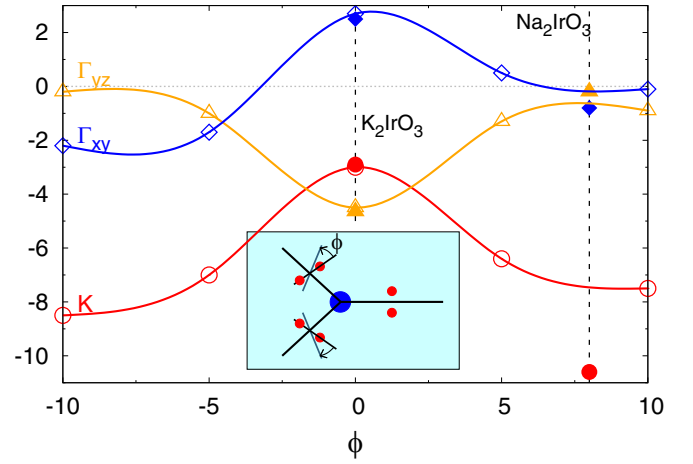


FIG. 2. Effects of  $C_3$  point-group symmetry on magnetic couplings: magnetic exchange couplings (in meV) as a function of the relative twist angle  $\phi$  of the O atoms away from the central  $\text{Ir}_2\text{O}_2$  plaquette (open symbols). The inset shows the definition of  $\phi$ , where Ir and the O atoms are represented by filled blue and red circles, respectively. The vertical dashed lines represent the approximate  $\phi$  values for  $\text{K}_2\text{IrO}_3$  and bond  $B1$  of  $\text{Na}_2\text{IrO}_3$ , and the corresponding magnetic couplings are shown by filled symbols. The solid lines are guides to the eye.

Presence of a smaller Na ion at the center of hexagons in the honeycomb layer in  $\text{Na}_2\text{IrO}_3$  leads to deviations from the  $120^\circ$  order. The O atoms reorganize themselves to lower the total energy. This is confirmed by comparing the total energy of  $\text{Na}_2\text{IrO}_3$  and an equivalent structure derived from  $\text{K}_2\text{IrO}_3$  such that the unit cell volume and Ir-Ir and Ir-O distances for these two structures are comparable (see Appendix A).  $\text{Na}_2\text{IrO}_3$  is found to be approximately 18 meV/atom lower in energy, thus establishing that the presence of larger intra-honeycomb-layer K ions leads to constraints in the relative orientation of the O atoms which, in turn, leads to large  $\Gamma$ 's. Similar nearly  $120^\circ$  arrangement for the O-O links is also found in the hyperhoneycomb compound  $\beta\text{-Li}_2\text{IrO}_6$  which also has somewhat larger  $\Gamma$ 's [18].

These results suggest that the real space  $C_3$  symmetry at the Ir sites is intricately related to the strong magnetic anisotropy. Even small deviations significantly influence the magnetic couplings, suggesting strong entanglement between real space and spin space. As a result, the NN magnetic interactions are strongly frustrated, highly anisotropic in spin space, and dominated by the  $\Gamma$  terms. While a sizable  $\Gamma_{yz}$  in such a situation is plausible for large trigonal distortions [39], it is interesting that unusually large  $\Gamma_{ij}$ 's in  $\text{K}_2\text{IrO}_3$  are realized even in the absence of sizable trigonal distortions.

It is important to note the fully anisotropic nature of the above  $J$ - $K$ - $\Gamma$  model. In comparison, some of the previously studied models consider only one component of  $\Gamma$  per bond [24–27]. On the other hand, in the fully anisotropic model for  $\text{Na}_2\text{IrO}_3$  [37] and  $\alpha\text{-RuCl}_3$  [11], the  $\Gamma$  terms turn out to be small. Nevertheless, they may have important consequences for magnetism [25–27]. In this regard, the implications of such large  $\Gamma$ 's, especially on the stability of a SL state, are particularly interesting.

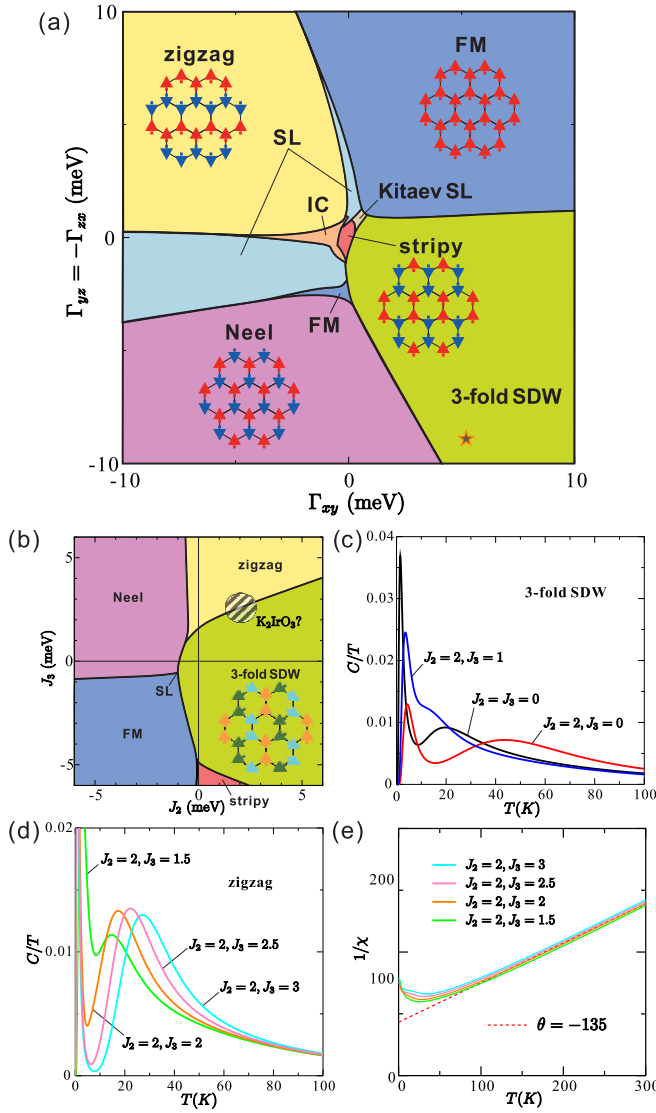


FIG. 3. Ground-state phase diagram by ED with a 24-site cluster: (a) in the  $\Gamma_{xy} - \Gamma_{yz}$  plane using the MRCI values of  $J$  and  $K$ ; (b) in the  $J_2 - J_3$  plane using the MRCI values of  $J$ ,  $K$ ,  $\Gamma_{xy}$ , and  $\Gamma_{yz}$ . Schematic spin configurations are also shown. The star symbol in (a) indicates the position of MRCI parameter set and it corresponds to the origin in (b). A realistic range for  $K_2\text{IrO}_3$  is located with shaded area in (b). Specific heat for the (c) threefold SDW and (d) zigzag phases, obtained by the ED calculations with a 12-site cluster. (e) Inverse magnetic susceptibility for the most likely realistic values of the extended range Heisenberg couplings  $J_2$  and  $J_3$ . The dotted line is  $\chi = 2.1/(T - \theta)$  with  $\theta = -135$  K.

#### D. Phase diagram for the $K$ - $J$ - $\Gamma$ model

We employ exact diagonalization (ED) calculations for the lattice realization of the fully anisotropic  $K$ - $J$ - $\Gamma$  model described by Eq. (1) on a 24-site cluster [5, 11, 14, 15]. The resulting magnetic phase diagram in the  $\Gamma_{xy} - \Gamma_{yz}$  plane is very rich due to competing magnetic interactions, shown in Fig. 3(a) where the MRCI values of  $J = 1.3$  and  $K = -6.3$  were fixed. It includes six ordered phases: ferromagnetic (FM), Néel, zigzag, stripy, threefold spin-density wave (SDW), and incommensurate (IC) (see Appendix D for details).

The most remarkable feature is that a ( $\Gamma$ -driven) SL state is found to be stable in a large region of the phase diagram, although a stripy state is realized at small values of  $\Gamma_{ij}$ . It suggests an alternative route to realize a SL state in spin-orbit driven Mott insulators on a honeycomb lattice. Especially, it is striking that a Kitaev-type SL is recovered between the FM and stripy phases (see Appendix D for details). The FM–Kitaev–SL–stripy path also appears when  $K/J$  is varied in the  $K$ - $J$  model [5], implying that the ratio  $K/J$  could be effectively controlled by the  $\Gamma$  terms. The remaining SL region is characterized as a frustration-induced “conventional” disordered state. A relatively wide region of SL phase exists for  $\Gamma_{ij} < 0$ , whereas, with increasing  $\Gamma_{ij} > 0$ , a SL state is stable only for small range, eventually leading to the FM order. This is consistent with an earlier work for the  $K$ - $\Gamma$  model [25].

Let us now consider the situation for  $K_2\text{IrO}_3$ . As indicated in Fig. 3(a), the *pure* MRCI parameter set ( $\Gamma_{xy} = 5.2$  meV,  $\Gamma_{yz} = -8.9$  meV) stands on the threefold SDW ordered phase. However, extended range Heisenberg couplings  $J_2$  and  $J_3$  are known to be important for honeycomb lattice spin-orbit driven Mott insulators [14]. Thus we obtain a phase diagram considering  $J_2$  and  $J_3$  couplings in addition to the MRCI parameter set, which is shown in Fig. 3(b). To estimate realistic values of  $J_2$  and  $J_3$  for  $K_2\text{IrO}_3$ , we turn towards the recent experimental observations [23]. Key features of the experimental specific heat are a broad maximum around 30 K and finite  $C/T$  down to 1.8 K. As shown in Figs. 3(c) and 3(d), the broad peak at  $\sim 30$  K can be numerically reproduced by setting  $J_2 \sim 2$  and  $J_3 \sim 2$ –3. Given these values, the system is just near the boundary between the zigzag and threefold SDW phases [see Fig. 3(b)]. Therefore, a strong competition between different orders is naturally expected, possibly explaining why no long-range order has been observed down to  $\sim 2$  K. Actually, the related Néel temperature is found to be  $T_N < 2$  K in the numerical calculations of specific heat. The corresponding inverse magnetic susceptibility for the zigzag state in an external magnetic field of 2 T perpendicular to the honeycomb planes leads to  $\theta \sim -135$  K [Fig. 3(e)], which is somewhat smaller than the experimental value of  $\theta \sim -180$  K [23]. Nonetheless, the zigzag state is the most probable ground state.

The synthesized  $K_x\text{Ir}_y\text{O}_2$  samples are nonstoichiometric and possess significant disorder in the form of vacancies in the K layer and presence of Ir/K occupancy at the centers of the hexagons in the honeycomb layers. As was recently shown [20, 36], disorder, especially vacancies and position of the interlayer cation, can significantly influence the magnetic couplings, and may possibly drive the system towards a SL state. However, a detailed study of such effects requires considerations beyond the scope of the present work.

#### III. CONCLUSIONS

In summary, we have investigated the magnetic interactions and the possibility of SL states in a structural model for honeycomb lattice Mott insulator featuring  $C_3$  symmetry at the TM ion sites by considering the recently proposed structural model for  $K_2\text{IrO}_3$ . We find that the resulting magnetic anisotropy is dominated by unusually large off-diagonal



anisotropic exchange couplings. Such large  $\Gamma$ 's are related to the  $C_3$  PG symmetry at the Ir sites, leading to constraints on the relative arrangement of O atoms. Despite small values of  $K$  and  $J$  as compared to  $\text{Na}_2\text{IrO}_3$ , the sizable  $K/J$  ratio motivates a fully anisotropic  $K$ - $J$ - $\Gamma$  model for  $\text{K}_2\text{IrO}_3$ , leading to strong magnetic frustration. Large quantum fluctuations suppress the magnetic ordering down to  $\sim 2$  K.

A fully anisotropic  $K$ - $J$ - $\Gamma$  Hamiltonian with large  $\Gamma$  terms is a generic feature of honeycomb Mott insulators with  $C_3$  PG symmetry at the TM-ion sites and has a rich magnetic phase diagram. We highlight that the relative sign of  $\Gamma_{ij}$  is critical for the stability of a SL state. The most remarkable aspect is the hitherto unexplored possibility that a SL can be stabilized even for small values of  $\Gamma < 0$  when  $K$  is ferromagnetic and the ratio  $|K/J|$  is relatively large ( $\gtrsim 5$ ). At the same time, the recognized FM-Kitaev-SL-stripy path of the  $K$ - $J$  model is also recovered at finite  $\Gamma_{ij}$ . While the search for a SL state in spin-orbit driven Mott insulators so far is focused on tuning the ratio  $K/J$ , our findings suggest that tuning the off-diagonal anisotropic couplings in materials with  $K < 0$  should also be promising.

## ACKNOWLEDGMENTS

We thank Yogesh Singh for the structural data which motivated this study, and Liviu Hozoi for helpful discussions. Part of this work is supported by the DFG through SFB 1143 Project No. A05. R.R. and M.R. acknowledge financial support from the European Union (ERDF) and the Free State of Saxony via the ESF Projects No. 100231947 and No. 100339533 [Young Investigators Group Computer Simulations for Materials Design (CoSiMa)]. We also thank Ulrike Nitzsche for technical support.

## APPENDIX A: DENSITY FUNCTIONAL CALCULATIONS

Spin polarized DFT calculations were performed using the Perdew-Burke-Ernzerhof (PBE) implementation [40] of the generalized gradient approximation (GGA) as implemented in the FPLO code [41], version 18.52 [42]. A  $k$  mesh with  $12 \times 12 \times 12$  intervals in the full Brillouin zone was used for numerical integration along with a linear tetrahedron method. For the electronic properties, the ‘‘atomic limit’’ (AL) implementation of the GGA+ $U$  functional was used. The spin-orbit effects were considered within the four-spinor formalism. For simplicity, the ferromagnetic state with spin quantization axis along  $[001]$  was considered.

### 1. Structure optimization

The structure optimization was performed for the internal parameters only, utilizing the space group  $P6_322$  (no. 182) and including the scalar relativistic corrections. The experimental values of the external parameters (lattice constants),  $a = b = 5.282$  Å,  $c = 13.544$  Å [22], were used. The residual force is less than 1 meV/Å on each atom. The optimal atomic positions are listed in Table II.

Note that the nearest neighbor octahedra are of slightly different sizes as implied by different Ir-O bond lengths. Therefore, at each Ir-Ir bond, inversion and mirror symmetry are absent. Consequently, the  $\text{Ir}_2\text{O}_{10}$  clusters do not have

TABLE II. Optimal atomic positions and related structural parameters in  $\text{K}_2\text{IrO}_3$ . The external parameters are kept fixed to the experimental value [22]: space group  $P6_322$  (no. 182) with  $a = b = 5.282$  Å and  $c = 13.544$  Å.

Atom	Wyck-pos	Coordinates ( $x/a, y/b, z/c$ )
Ir1	2b	(0, 0, 1/4)
Ir2	2c	(1/3, 2/3, 1/4)
K1	2d	(2/3, 1/3, 1/4)
K2	6g	(0.3404, 0.3404, 1/2)
O	12i	(0.3328, 0.0593, -0.3442)
Param.	Values	
$d_{\text{Ir-Ir}}$ (Å)	3.0496	
$d_{\text{Ir-O}}$ (Å)	2.065, 2.069	
$d_{\text{Ir-layers}}$ (Å)	6.77	
$\angle \text{Ir-Ir-Ir}$	$120^\circ$	
$\angle \text{Ir-O-Ir}$	$95.06^\circ$	

$C_{2h}$  symmetry. However, deviation from the  $C_{2h}$  symmetry is only marginal as the Ir-O bond lengths differ by  $\lesssim 0.19\%$ . Therefore,  $C_{2h}$  symmetry is a reasonable approximation and is used in the quantum chemistry calculations.

### 2. Electronic properties

Figure 4 shows the total and partial density of states (DOS) for  $\text{K}_2\text{IrO}_3$  with  $U = 1.2$  eV and  $J = 0.3$  eV applied to the Ir-5d states. For comparison, the total DOS for  $\text{Na}_2\text{IrO}_3$  with the reported lattice parameters [6] and optimized internal parameters, and with the same  $U$  and  $J$  values for the Ir-5d states, is also shown. The  $d$ - $t_{2g}$  and  $d$ - $e_g$  states are also marked. The clear splitting of the  $d$ - $t_{2g}$  bands into  $j_{\text{eff}} = 3/2$  and  $1/2$  states is evident, implying that  $\text{K}_2\text{IrO}_3$  is a spin-orbit driven

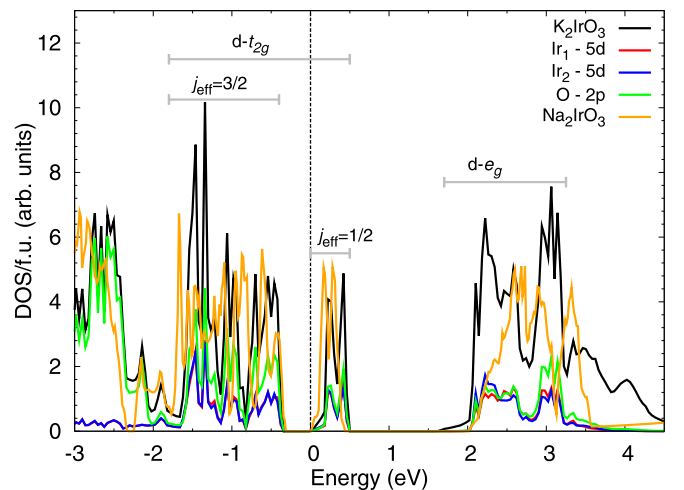


FIG. 4. Total (spin-up + spin-down) density of states (DOS) per formula unit (f.u.) for the spin-orbit driven Mott insulator  $\text{K}_2\text{IrO}_3$  along with the contributions of Ir-5d and O-2p states as obtained within the GGA+ $U$  scheme and considering spin-orbit effects, with  $U_{\text{Ir-5d}} = 1.2$  eV and  $J_{\text{Ir-5d}} = 0.3$  eV. For comparison, the total DOS for  $\text{Na}_2\text{IrO}_3$  with the same  $U$  and  $J$  values is also shown. The Fermi energy is shown by dashed vertical line.

TABLE III. Comparison of the ground-state magnetic properties of  $\text{K}_2\text{IrO}_3$  and  $\text{Na}_2\text{IrO}_3$  obtained within the GGA+ $U$  scheme with spin-orbit coupling.  $U = 1.2$  eV and  $J = 0.3$  eV was applied to the Ir-5d states.

Param.	$\text{K}_2\text{IrO}_3$	$\text{Na}_2\text{IrO}_3$
$m_S^{\text{Ir}} (\mu_B)$	0.574, 0.569	0.431
$m_S^{\text{O}} (\mu_B)$	0.095	0.062, 0.061
$m_S^{\text{K/Na}} (\mu_B)$	0.005, 0.002	0.003, 0.001
$m_S^{\text{tot}} (\text{per f.u.}, \mu_B)$	0.864	0.620
$m_L^{\text{Ir}} (\mu_B)$	0.862, 0.855	0.584

Mott insulator. The ground-state properties, especially the magnetic moments, are comparable with  $\text{Na}_2\text{IrO}_3$ , as shown in Table III.

### 3. Comparison with an equivalent $\text{Na}_2\text{IrO}_3$ structure—role of K ions

To ascertain the relation between the  $C_3$  point-group symmetry at the Ir sites and the presence of the K ions at the center of the hexagons in the honeycomb layer, we performed DFT calculations with the following assertion: if the  $C_3$  point-group symmetry is a direct consequence of the larger  $\text{K}^+$  ions, the presence of a smaller nonmagnetic cation, such as  $\text{Na}^+$ , would allow the O atoms to reorganize themselves to a lower symmetry structure and, subsequently, lower the total energy. Indeed,  $\text{Na}_2\text{IrO}_3$  crystallizes in the space group  $C2/m$  [6], which does not have the relative  $120^\circ$  arrangement of the O-O links [shown in Fig. 1(b) in the main text].

The truthfulness of this assertion was checked by comparing the ground-state energies (within GGA) of the known structure of  $\text{Na}_2\text{IrO}_3$  [6], but with optimized atomic positions, with an equivalent structure derived from  $\text{K}_2\text{IrO}_3$  with the  $C_3$  point-group symmetry at the Ir sites, labeled as  $\text{Na}_2\text{IrO}_3^*$ . The equivalency between the two structures corresponds to

comparable Ir-Ir and Ir-O distances and the unit cell volume.  $\text{Na}_2\text{IrO}_3^*$  was obtained from  $\text{K}_2\text{IrO}_3$  in the following steps.

- (1) Replace all K ions by Na ions.
- (2) Tune  $a$  (and  $b$ ) such that the Ir-Ir distances are comparable to that of  $\text{Na}_2\text{IrO}_3$ .
- (3) Reduce  $c$  such that the unit cell volumes match while the interlayer separations and the Ir-O distances are comparable to  $\text{Na}_2\text{IrO}_3$ .
- (4) Optimize the atomic positions of the resulting structure.

The atomic positions and structural details of both the structures are presented in Table IV.

## APPENDIX B: QUANTUM CHEMISTRY CALCULATIONS

To determine the strength of NN magnetic couplings for the DFT-optimized structure, quantum chemistry calculations were performed on a material model consisting of a two NN edge shared octahedra unit  $\text{Ir}_2\text{O}_{10}$ . Additionally, the four octahedra sharing edge with the central unit along with eighteen NN K ions were also explicitly included in the calculations to account for the finite charge distribution in the immediate neighborhood. The remaining solid-state surroundings were modeled by arrays of point charges such that they reproduce the ionic Madelung potential in the cluster region. Energy-consistent relativistic pseudopotentials along with quadruple-zeta basis functions were used for the Ir ions [43] of the central unit, while all-electron quintuple-zeta basis sets were employed for the bridging O ligands [44]. The remaining O atoms in the two-octahedra central region were described using all-electron basis sets of triple-zeta quality [44].  $\text{Ir}^{4+}$  sites belonging to the octahedra adjacent to the reference unit were described as closed-shell  $\text{Pt}^{4+}t_{2g}^6$  ions, using relativistic pseudopotentials and valence triple-zeta basis functions [43]. Ligands belonging to these adjacent octahedra which are not shared with the central (reference) unit were modeled with minimal all-electron atomic-natural-orbital basis sets [45]. All occupied shells of NN  $\text{K}^+$  sites were represented by using

TABLE IV. Comparison of the structural parameters between  $\text{Na}_2\text{IrO}_3^*$  and  $\text{Na}_2\text{IrO}_3$ . “\*” denotes that this structure was obtained from  $\text{K}_2\text{IrO}_3$  such that the Ir-Ir distances and the unit cell volume are comparable with  $\text{Na}_2\text{IrO}_3$ .

Atom	$\text{Na}_2\text{IrO}_3^*$	$\text{Na}_2\text{IrO}_3$
Ir1	(0, 0, 1/4)	(0, -0.3338, 0)
Ir2	(1/3, 2/3, 1/4)	
Na1	(2/3, 1/3, 1/4)	(0, 0, 0)
Na2	(0.3414, 0.3414, 1/2)	(0, -0.1598, 1/2)
Na3		(0.3404, 0.3404, 1/2)
O	(0.3332, 0.0291, 0.6449)	(-0.25284, 0.18314, -0.21001)
Param.		
Space group	$P6_322$ (no. 182)	$C2/m$ (no. 12)
Volume/f.u. ( $\text{\AA}^3$ )	67.646	67.646
Energy difference/f.u. (meV)	107.89	0.0
$d_{\text{Ir-Ir}}$ ( $\text{\AA}$ )	3.12	3.12, 3.14
$d_{\text{Ir-O}}$ ( $\text{\AA}$ )	2.061, 2.0623	2.054, 2.061
$d_{\text{Ir-layers}}$ ( $\text{\AA}$ )	5.338	5.614
$\angle \text{Ir-Ir-Ir}$	$120^\circ$	$120.12^\circ, 119.76^\circ$
$\angle \text{Ir-O-Ir}$	$98.48^\circ$	$99.344^\circ$

TABLE V. Atomic positions of the atoms in the  $\text{Ir}_2\text{O}_{10}$  clusters for different values of the twist angle  $\phi$ .

Atom.	$x$ (Å)	$y$ (Å)	$z$ (Å)
$\phi = 0$			
Ir1	0.000000	0.000000	0.000000
Ir2	3.049560	0.000000	0.000000
O1	1.524780	0.759692	1.170942
O2	1.524780	-0.759692	-1.170942
O3	-1.420303	0.940652	1.170942
O4	-0.104478	1.700344	-1.170942
O5	-0.104477	-1.700344	1.170942
O6	-1.420303	-0.940652	-1.170942
O7	4.469863	0.940652	1.170942
O8	3.154038	1.700344	-1.170942
O9	3.154037	-1.700345	1.170942
O10	4.469863	-0.940652	-1.170942
$\phi = 10^\circ$			
Ir1	0.000000	0.000000	0.000000
Ir2	3.049560	0.000000	0.000000
O1	1.524780	0.759692	1.170942
O2	1.524780	-0.759692	-1.170942
O3	-1.476267	1.060668	1.170942
O4	-0.048513	1.580328	-1.170942
O5	-0.048513	-1.580328	1.170942
O6	-1.476267	-1.060668	-1.170942
O7	4.525827	1.060668	1.170942
O8	3.098073	1.580328	-1.170942
O9	3.098073	-1.580328	1.170942
O10	4.525827	-1.060668	-1.170942

pseudopotentials and each of the K 4s orbitals were described with a single basis function [46]. All quantum chemistry computations were performed using the quantum chemistry package MOLPRO.

In the first step, complete-active-space self-consistent-field (CASSCF) calculations [2] were carried out for an average of the lowest nine singlet and nine triplet states, essentially of  $t_{2g}^5 - t_{2g}^5$  character. Since CASSCF calculations also account for superexchange processes of  $t_{2g}^6 - t_{2g}^4$  type in addition to NN  $t_{2g}^5 - t_{2g}^5$  direct exchange, CASSCF wave functions also consist of a finite weight contribution from intersite excitations of  $t_{2g}^6 - t_{2g}^4$  type. Single and double excitations from the transition metal  $d$  ( $t_{2g}$ ) and bridging-ligand  $p$  valence shells were accounted for in the subsequent MRCI computations. The low-lying nine singlet and nine triplet states were considered in the spin-orbit treatment, in both CASSCF and MRCI calculations. In the next step, the *ab initio* quantum-chemistry data were mapped onto an effective spin Hamiltonian [Eq. (1) in the main text], which involves only the lowest four spin-orbit states, associated with the different possible couplings of the two NN 1/2 pseudospins. The other 32 spin-orbit levels arising from the  $t_{2g}^5 - t_{2g}^5$  configuration involve  $j_{\text{eff}} \approx 3/2$  to  $j_{\text{eff}} \approx 1/2$  excitations and lie at significantly higher energy [14,35]. The mapping was performed following the procedure described in Ref. [11]. The magnetic couplings shown in Table I in the main text are obtained by following this procedure.

## APPENDIX C: TESTS FOR THE ROLE OF $C_3$ POINT-GROUP SYMMETRY

To further test our claim that  $C_3$  point-group symmetry at each Ir site is crucial to the strength of off-diagonal exchange couplings, we performed an additional set of quantum chemistry calculations using an edge shared octahedra unit  $[\text{Ir}_2\text{O}_{10}]^{2-}$  as the central region. We begin with a  $[\text{Ir}_2\text{O}_{10}]^{2-}$  structural unit obtained from an idealized crystalline structure displaying  $C_3$  point-group symmetry about an axis perpendicular to the honeycomb plane (“ $c$ ” axis) at each Ir site. The structural unit, therefore, has  $C_{2h}$  point-group symmetry. All adjacent Ir and K sites were modeled as identical point charges to make the whole system charge neutral. Using this model, *ab initio* spin-orbit calculations at the MRCI level were carried out to obtain effective coupling parameters.

In the next step, we reduced the symmetry of the  $[\text{Ir}_2\text{O}_{10}]^{2-}$  structural unit such that only  $C_{2h}$  symmetry of the cluster is retained, while the  $C_3$  point-group symmetry at each Ir site is lost. This was obtained by keeping the central plaquette unchanged (i.e., no modifications to Ir-Ir or Ir-O bond lengths and Ir-O-Ir bond angles within this plaquette). However, the other sets of O atoms (representing the other two plaquettes at each site) were rotated about an axis passing through the center of the O-O links and perpendicular to the hexagonal plane spanned by the Ir atoms. The positions of all such O atoms are connected by the twofold rotation about the Ir-Ir axis and the mirror plane perpendicular to the Ir-Ir bond, which defines the  $C_{2h}$  symmetry. The resulting structures can therefore be characterized by a single “twist angle”  $\phi$  (see Fig. 2, main text). The structural positions of all the atoms for  $\phi = 0$  and  $\phi = 10^\circ$  is presented in Table V. The magnetic couplings were then obtained for different structures corresponding to different values of  $\phi$  by keeping the point charge embedding same as in the first step ( $\phi = 0$ ).

The modification of the O sites corresponding to the NN plaquette affects the Ir  $d$  orbitals in a way that results in an increase in Kitaev exchange, while decreasing the off-diagonal exchange components at the same time. MRCI spin-orbit results obtained for two site clusters with varying  $\phi$  are shown in Fig. 2 in the main text. The model structure with  $\phi = 0$  corresponds to the crystalline structure proposed for  $\text{K}_2\text{IrO}_3$ , while the model structure with  $\phi = 10^\circ$  can be compared with the crystal structure of  $\text{Na}_2\text{IrO}_3$ .

Basis sets of the same quality as discussed in the previous section were used for the structural unit in these calculations. Additionally, to access the reliability of these test calculations we performed checks by changing the embedding to the one with a lower symmetry arising due to the distortions. We find that the qualitative trend obtained in these calculations remains the same as shown in Fig. 2 in the main text.

## APPENDIX D: EXACT DIAGONALIZATION CALCULATIONS

### 1. Static spin-structure factor

To investigate the lattice magnetic structure, we calculated the static spin-structure factor

$$S(\mathbf{Q}) = \frac{1}{N} \sum_{ij} \langle \tilde{\mathbf{S}}_i \cdot \tilde{\mathbf{S}}_j \rangle \exp[i\mathbf{Q} \cdot (\mathbf{r}_i - \mathbf{r}_j)], \quad (\text{D1})$$

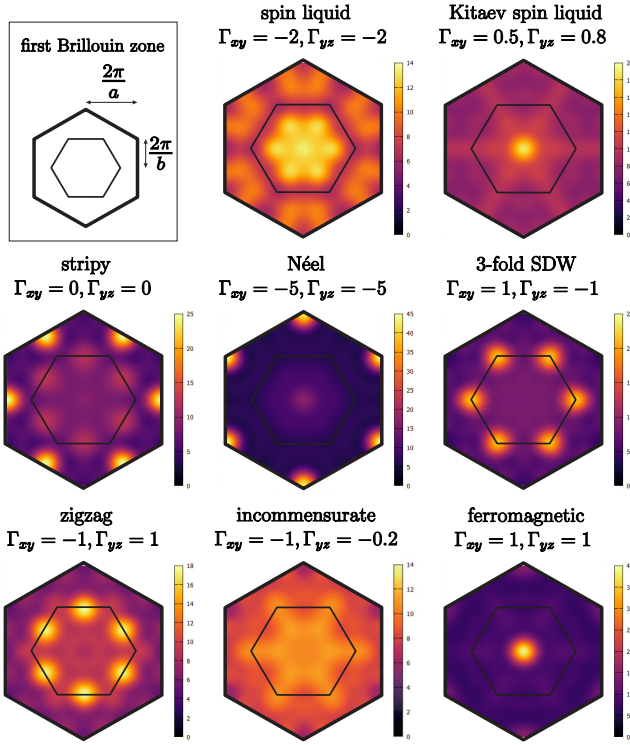


FIG. 5. Spin-structure factor  $S(\mathbf{Q})$  for representative momenta in different phases.

where  $N$  is the number of sites in a periodic cluster and  $\mathbf{r}_i$  is the position of site  $i$ . In Fig. 5 we show the structure factors  $S(\mathbf{Q})$  for representative momenta (first Brillouin zone) in different phases. Typical  $\Gamma_{xy}$  and  $\Gamma_{yz}$  values were chosen for each phase. For the ordered phases the magnetic structure can be determined from the reciprocal-space Bragg-peak positions. In the incommensurate (IC) phase the Bragg-peak positions are shifted with varying  $\Gamma_{xy}$  and  $\Gamma_{yz}$  if the system is large enough. However, our system size is 24 and only discrete momenta are allowed. In such a case, usually, the dominant IC Bragg-peak position is moved from an IC momentum to another by transferring the weight with varying  $\Gamma_{xy}$  and  $\Gamma_{yz}$ . Also, it is worth noting the difference between the structure factors of the “conventional” (non-Kitaev-type) and Kitaev-type SL states. In the conventional SL phase  $S(\mathbf{Q})$  is structureless and the weight is widely distributed over the reciprocal space, reflecting a disordered spin state, whereas in the Kitaev-type SL phase the weight is very small for the whole  $\mathbf{Q}$  range because the spin-spin correlations except for the nearest-neighbor bond are very small. A peak at  $\mathbf{Q} = \mathbf{0}$  is due to the finite-size effect. Further discussion about the spin-spin correlations is given below.

## 2. Quantum phase transition

To find the phase boundaries, we checked the second derivatives of the ground-state energy  $E_0/N$  and the total spin  $2S_{\text{tot}}/N$  with respect to particular parameters. In Fig. 6(b) we illustrate four phase transitions (SL–IC–stripy–Kitaev SL–FM) with varying  $\Gamma_{xy}$  and  $\Gamma_{yz}$  along the dashed

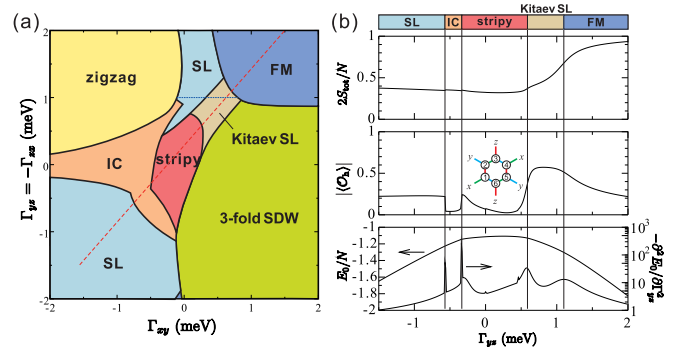


FIG. 6. (a) Ground-state phase diagram around  $\Gamma_{xy} = \Gamma_{yz} = 0$ , extracted from Fig. 3 in the main text. (b) Representative physical quantities for the 24-site periodic cluster as a function of  $\Gamma_{yz}$  along red dashed line ( $\Gamma_{yz} = \frac{8}{7}\Gamma_{xy} + \frac{2}{7}$ ) in (a). Top: total spin. Middle: expectation value of the hexagonal plaquette operator. Bottom: ground-state energy per site  $E_0/N$  and its second derivative  $-\partial^2 E_0 / \partial \Gamma_{yz}^2$ .

line in Fig. 6(a). The critical  $\Gamma$  values were estimated from the peak positions in the second derivative of the ground-state energy  $-\partial^2 E_0 / \partial \Gamma_{yz}^2$ ; the SL–IC–stripy–Kitaev SL–FM phase transitions occur at  $(\Gamma_{xy}, \Gamma_{yz}) = (-0.74875, -0.57)$ ,  $(-0.54750, -0.34)$ ,  $(0.25750, 0.58)$ , and  $(0.71250, 1.10)$ , respectively. The former two transitions are of the first order, and the latter two are of the second order or continuous. Furthermore, we considered the hexagonal plaquette operator to check the topological property of the spin liquid state. The plaquette operator is an indicative quantity for the Kitaev-type spin liquid. It is defined as [47]

$$O_h = 2^6 \tilde{S}_1^x \tilde{S}_2^y \tilde{S}_3^z \tilde{S}_4^x \tilde{S}_5^y \tilde{S}_6^z, \quad (\text{D2})$$

where the labeling of links and sites is denoted in the middle panel of Fig. 6(b). In the pure Kitaev limit ( $K \gg J, \Gamma$ ) the operator [Eq. (D2)] commutes with the Hamiltonian and the expectation value of  $\langle O_h \rangle$  is exactly  $\pm 1$ . It is also known that it goes rapidly down to  $\langle O_h \rangle \sim 0$  away from the Kitaev spin liquid regions [11]. As shown in Fig. 6(b), the plaquette operator is significantly enhanced in a spin liquid region at

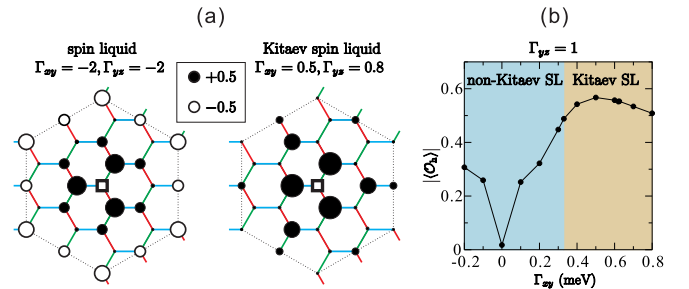


FIG. 7. Spin-spin correlation function  $\langle \tilde{S}_i \cdot \tilde{S}_j \rangle$  for non-Kitaev and Kitaev SL states in our phase diagram [Fig. 6(a)]. The reference site  $i$  is denoted by open square and the value of  $\langle \tilde{S}_i \cdot \tilde{S}_j \rangle$  at site  $j$  is expressed by a circle. The filled and open circles mean positive and negative values of  $\langle \tilde{S}_i \cdot \tilde{S}_j \rangle$ , respectively. The diameter of each circle is proportional to the magnitude, i.e.,  $|\langle \tilde{S}_i \cdot \tilde{S}_j \rangle|$ . (b) Expectation value of the hexagonal plaquette operator  $|\langle O_h \rangle|$  as a function of  $\Gamma_{xy}$  at  $\Gamma_{yz} = 1$  fixed [along blue dotted line in Fig. 6(a)].



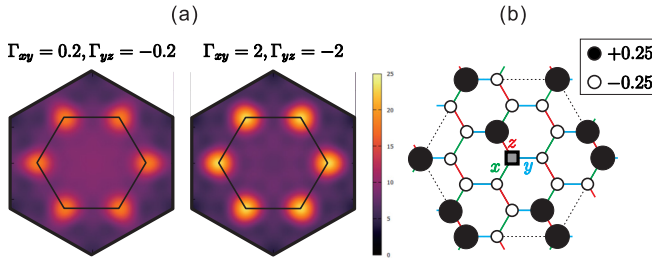


FIG. 8. (a) Spin-structure factor  $S(\mathbf{Q})$  for  $\Gamma_{xy} = 0.2$ ,  $\Gamma_{yz} = -0.2$  and  $\Gamma_{xy} = 2$ ,  $\Gamma_{yz} = -2$ , where the system is in the threefold SDW state. (b) Real-space spin-spin correlation function  $\langle \tilde{\mathbf{S}}_i \cdot \tilde{\mathbf{S}}_j \rangle$  for a threefold SDW state ( $\Gamma_{xy} = 5$ ,  $\Gamma_{yz} = -5$ ). The reference site  $i$  is denoted by open square and the value of  $\langle \tilde{\mathbf{S}}_i \cdot \tilde{\mathbf{S}}_j \rangle$  at site  $j$  is expressed by a circle. The filled and open circles mean positive and negative values of  $\langle \tilde{\mathbf{S}}_i \cdot \tilde{\mathbf{S}}_j \rangle$ , respectively. The diameter of each circle is proportional to the magnitude, i.e.,  $|\langle \tilde{\mathbf{S}}_i \cdot \tilde{\mathbf{S}}_j \rangle|$ . To detect the symmetry-broken state, the reference site is pinned by an infinite local magnetic field.

$0.25750 < \Gamma_{xy} < 0.71250$ ,  $0.58 < \Gamma_{yz} < 1.10$ . Thus we conclude that this spin liquid is of the Kitaev type. This is also consistent with the almost weightless  $S(\mathbf{Q})$  shown above.

### 3. Difference between Kitaev and non-Kitaev spin liquids

Sometimes, it is not easy to distinguish between Kitaev and non-Kitaev SL states because the phase transition is rather crossoverlike. Nevertheless, they may be identified by looking at their spin-spin correlations (spin structure factor) and expectation value of the plaquette operator  $\langle O_h \rangle$ .

In general, the Kitaev SL state is characterized by a rapid decay of the spin-spin correlations: in the Kitaev limit, only the NN correlations are finite and longer-range ones are zero; accordingly, as shown in Fig. 5, the static spin structure factor has a single  $\mathbf{Q} = \mathbf{0}$  peak, the weight of which is much smaller than that for a FM state, in a finite-size cluster. On the other

hand, the spin-spin correlations for a non-Kitaev SL are also not long ranged but the decay lengths are typically much larger, i.e., like a power-law decay, than that for the Kitaev SL; thus a structureless  $S(\mathbf{Q})$  is obtained. This can be simply confirmed by considering the spin-spin correlations in the real space. In Fig. 7(a) the real-space spin-spin correlations for non-Kitaev and Kitaev SL states are compared. We can obviously see that the correlation for Kitaev SL decays very rapidly and it is very small for longer distances than one lattice spacing; that for non-Kitaev SL decays much more slowly with distance.

We also show an expectation value of the hexagonal plaquette operator  $|\langle O_h \rangle|$  around the phase boundary between non-Kitaev and Kitaev SL phases in Fig. 7(b). A steep increase of  $|\langle O_h \rangle|$  from non-Kitaev towards Kitaev SL phases is clearly seen.

### 4. Spin structure of the threefold SDW state

As shown in our phase diagram [Fig. 3(a) in the main text], the ground state for a wide range of  $\Gamma_{xy} >$  and  $\Gamma_{yz} <$  is characterized as a threefold SDW phase. The spin-structure factor  $S(\mathbf{Q})$  for  $\Gamma_{xy} = 0.2$ ,  $\Gamma_{yz} = -0.2$  and  $\Gamma_{xy} = 2$ ,  $\Gamma_{yz} = -2$  are shown in Fig. 8(a). The set  $\Gamma_{xy} = 0.2$ ,  $\Gamma_{yz} = -0.2$  belongs to the threefold SDW ground state but is in the vicinity of the neighboring stripy phase. Therefore, the peak structure in  $S(\mathbf{Q})$  is still somewhat blurred. Roughly speaking, this phase is more stabilized as  $\Gamma_{xy} \approx -\Gamma_{yz}$  increases. We have also confirmed that the threefold SDW state is maintained up to the limit of  $\Gamma_{xy} \approx -\Gamma_{yz} = \infty$ .

In order to see the spin structure of the threefold SDW state, we calculate the real-space spin-spin correlation function  $\langle \tilde{\mathbf{S}}_i \cdot \tilde{\mathbf{S}}_j \rangle$ . The result is plotted in Fig. 8(b). A pinning is achieved by applying an infinite-strength magnetic field along the  $z$  axis on a site [referred to as a reference site in Fig. 8(b)] to directly detect a symmetry-broken state with a periodic cluster. We can clearly see a SDW structure with threefold oscillation perpendicular to the  $z$  bond.

- [1] A. Banerjee, C. Bridges, J.-Q. Yan, A. Aczel, L. Li, M. Stone, G. Granroth, M. Lumsden, Y. Yiu, and J. Knolle, *Nat. Mater.* **15**, 733 (2016).
- [2] T. Helgaker, P. Jørgensen, and J. Olsen, *Molecular Electronic-Structure Theory* (Wiley, Chichester, 2000).
- [3] J. Kim, M. Daghofer, A. H. Said, T. Gog, J. van den Brink, G. Khaliullin, and B. J. Kim, *Nat. Commun.* **5**, 4453 (2014).
- [4] A. Lupascu, J. P. Clancy, H. Gretarsson, Z. Nie, J. Nichols, J. Terzic, G. Cao, S. S. A. Seo, Z. Islam, M. H. Upton, J. Kim, D. Casa, T. Gog, A. H. Said, V. M. Katukuri, H. Stoll, L. Hozoi, J. van den Brink, and Y.-J. Kim, *Phys. Rev. Lett.* **112**, 147201 (2014).
- [5] J. Chaloupka, G. Jackeli, and G. Khaliullin, *Phys. Rev. Lett.* **105**, 027204 (2010).
- [6] S. K. Choi, R. Coldea, A. N. Kolmogorov, T. Lancaster, I. I. Mazin, S. J. Blundell, P. G. Radaelli, Y. Singh, P. Gegenwart, K. R. Choi, S.-W. Cheong, P. J. Baker, C. Stock, and J. Taylor, *Phys. Rev. Lett.* **108**, 127204 (2012).
- [7] S. H. Chun, J.-W. Kim, J. Kim, H. Zheng, C. C. Stoumpos, C. D. Malliakas, J. F. Mitchell, K. Mehlawat, Y. Singh, Y. Choi, T. Gog, A. Al-Zein, M. M. Sala, M. Krisch, J. Chaloupka, G. Jackeli, G. Khaliullin, and B. J. Kim, *Nat. Phys.* **11**, 462 (2015).
- [8] Y. Singh, S. Manni, J. Reuther, T. Berlijn, R. Thomale, W. Ku, S. Trebst, and P. Gegenwart, *Phys. Rev. Lett.* **108**, 127203 (2012).
- [9] I. I. Mazin, S. Manni, K. Foyevtsova, H. O. Jeschke, P. Gegenwart, and R. Valentí, *Phys. Rev. B* **88**, 035115 (2013).
- [10] K. W. Plumb, J. P. Clancy, L. J. Sandilands, V. V. Shankar, Y. F. Hu, K. S. Burch, H. Y. Kee, and Y. J. Kim, *Phys. Rev. B* **90**, 041112(R) (2014).
- [11] R. Yadav, N. A. Bogdanov, V. M. Katukuri, S. Nishimoto, J. van den Brink, and L. Hozoi, *Sci. Rep.* **6**, 37925 (2016).
- [12] I. Kimchi and Y. Z. You, *Phys. Rev. B* **84**, 180407(R) (2011).
- [13] J. G. Rau, E. K.-H. Lee, and H.-Y. Kee, *Phys. Rev. Lett.* **112**, 077204 (2014).

- [14] V. M. Katukuri, S. Nishimoto, V. Yushankhai, A. Stoyanova, H. Kandpal, S. Choi, R. Coldea, I. Rousochatzakis, L. Hozoi, and J. van den Brink, *New J. Phys.* **16**, 013056 (2014).
- [15] S. Nishimoto, V. M. Katukuri, V. Yushankhai, H. Stoll, U. K. Rößler, L. Hozoi, I. Rousochatzakis, and J. van den Brink, *Nat. Commun.* **7**, 10273 (2016).
- [16] A. Banerjee, P. Lampen-Kelley, J. Knolle, C. Balz, A. A. Aczel, B. Winn, Y. Liu, D. Pajerowski, J. Yan, C. A. Bridges *et al.*, *npj Quantum Mater.* **3**, 8 (2018).
- [17] G. Bastien, G. Garbarino, R. Yadav, F. J. Martinez-Casado, R. Beltran Rodriguez, Q. Stahl, M. Kusch, S. P. Limandri, R. Ray, P. Lampen-Kelley, D. G. Mandrus, S. E. Nagler, M. Roslova, A. Isaeva, T. Doert, L. Hozoi, A. U. B. Wolter, B. Buchner, J. Geck, and J. van den Brink, *Phys. Rev. B* **97**, 241108(R) (2018).
- [18] M. Majumder, R. S. Manna, G. Simutis, J. C. Orain, T. Dey, F. Freund, A. Jesche, R. Khasanov, P. K. Biswas, E. Bykova, N. Dubrovinskaya, L. S. Dubrovinsky, R. Yadav, L. Hozoi, S. Nishimoto, A. A. Tsirlin, and P. Gegenwart, *Phys. Rev. Lett.* **120**, 237202 (2018).
- [19] G. Simutis, N. Barbero, K. Rolf, P. Leroy-Calatayud, K. Mehlawat, R. Khasanov, H. Luetkens, E. Pomjakushina, Y. Singh, H.-R. Ott, J. Mesot, A. Amato, and T. Shiroka, *Phys. Rev. B* **98**, 104421 (2018).
- [20] R. Yadav, R. Ray, M. S. Eldeeb, S. Nishimoto, L. Hozoi, and J. van den Brink, *Phys. Rev. Lett.* **121**, 197203 (2018).
- [21] A. Koitzsch, C. Habenicht, E. Müller, M. Knupfer, B. Büchner, S. Kretschmer, M. Richter, J. van den Brink, F. Börrnert, D. Nowak, A. Isaeva, and T. Doert, *Phys. Rev. Materials* **1**, 052001 (2017).
- [22] R. D. Johnson, I. Broeders, K. Mehlawat, Y. Li, Y. Singh, R. Valentí, and R. Coldea, *arXiv:1908.04584*.
- [23] K. Mehlawat and Y. Singh, *arXiv:1908.08475*.
- [24] I. Rousochatzakis and N. B. Perkins, *Phys. Rev. Lett.* **118**, 147204 (2017).
- [25] A. Catuneanu, Y. Yamaji, G. Wachtel, Y. B. Kim, and H.-Y. Kee, *npj Quantum Mater.* **3**, 23 (2018).
- [26] P. Lampen-Kelley, S. Rachel, J. Reuther, J. Q. Yan, A. Banerjee, C. A. Bridges, H. B. Cao, S. E. Nagler, and D. Mandrus, *Phys. Rev. B* **98**, 100403(R) (2018).
- [27] M. Gohlke, G. Wachtel, Y. Yamaji, F. Pollmann, and Y. B. Kim, *Phys. Rev. B* **97**, 075126 (2018).
- [28] H. Gretarsson, J. P. Clancy, X. Liu, J. P. Hill, E. Bozin, Y. Singh, S. Manni, P. Gegenwart, J. Kim, A. H. Said, D. Casa, T. Gog, M. H. Upton, H.-S. Kim, J. Yu, V. M. Katukuri, L. Hozoi, J. van den Brink, and Y.-J. Kim, *Phys. Rev. Lett.* **110**, 076402 (2013).
- [29] G. Jackeli and G. Khaliullin, *Phys. Rev. Lett.* **102**, 017205 (2009).
- [30] A. Abragam and B. Bleaney, *Electron Paramagnetic Resonance of Transition Ions* (Clarendon Press, London, 1970).
- [31] B. J. Kim, H. Jin, S. J. Moon, J.-Y. Kim, B.-G. Park, C. S. Leem, J. Yu, T. W. Noh, C. Kim, S.-J. Oh, J.-H. Park, V. Durairaj, G. Cao, and E. Rotenberg, *Phys. Rev. Lett.* **101**, 076402 (2008).
- [32] N. A. Bogdanov, V. M. Katukuri, J. Romhányi, V. Yushankhai, V. Kataev, B. Büchner, J. van den Brink, and L. Hozoi, *Nat. Commun.* **6**, 7306 (2015).
- [33] R. Yadav, M. Pereiro, N. A. Bogdanov, S. Nishimoto, A. Bergman, O. Eriksson, J. van den Brink, and L. Hozoi, *Phys. Rev. Materials* **2**, 074408 (2018).
- [34] N. A. Bogdanov, V. M. Katukuri, H. Stoll, J. van den Brink, and L. Hozoi, *Phys. Rev. B* **85**, 235147 (2012).
- [35] V. M. Katukuri, R. Yadav, L. Hozoi, S. Nishimoto, and J. van den Brink, *Sci. Rep.* **6**, 29585 (2016).
- [36] R. Yadav, M. S. Eldeeb, R. Ray, S. Aswartham, M. I. Sturza, S. Nishimoto, J. van den Brink, and L. Hozoi, *Chem. Sci.* **10**, 1866 (2019).
- [37] R. Yadav, S. Rachel, L. Hozoi, J. van den Brink, and G. Jackeli, *Phys. Rev. B* **98**, 121107(R) (2018).
- [38] S. M. Winter, Y. Li, H. O. Jeschke, and R. Valentí, *Phys. Rev. B* **93**, 214431 (2016).
- [39] J. Chaloupka and G. Khaliullin, *Phys. Rev. B* **92**, 024413 (2015).
- [40] J. P. Perdew, K. Burke, and M. Ernzerhof, *Phys. Rev. Lett.* **77**, 3865 (1996); Erratum: **78**, 1396 (1997).
- [41] K. Koepnik and H. Eschrig, *Phys. Rev. B* **59**, 1743 (1999).
- [42] <https://www.fpl.de>.
- [43] D. Figgen, K. A. Peterson, M. Dolg, and H. Stoll, *J. Chem. Phys.* **130**, 164108 (2009).
- [44] T. H. Dunning, *J. Chem. Phys.* **90**, 1007 (1989).
- [45] K. Pierloot, B. Dumez, P.-O. Widmark, and B. O. Roos, *Theor. Chim. Acta* **90**, 87 (1995).
- [46] P. Fuentealba, H. Preuss, H. Stoll, and L. V. Szentpály, *Chem. Phys. Lett.* **89**, 418 (1982).
- [47] A. Kitaev, *Ann. Phys. (NY)* **321**, 2 (2006).